GSA Data Repository item 2018275 https://doi.org/10.1130/G45158.1

Anisotropic magnetite growth in remagnetized limestones: tectonic constraints and implications for basin history

Pablo Calvín[1], Juan J. Villalaín[1], and Antonio M. Casas-Sainz[2]

[1]Laboratorio de Paleomagnetismo, Universidad de Burgos, Av/ Cantabria s/n, 9006 Burgos, Spain.

[2]Geotransfer Research Group (IUCA), Universidad de Zaragoza, C/ Pedro Cerbuna 12, 50009 Zaragoza, Spain.

Table of Contents

A1. List of supplementary tables and figures

Figure DR1. Charts illustrating the analysis of remagnetization directions using the small circle intersection (SCI) method and bedding restoration at the remagnetization acquisition time. (a) The cone defined by a paleomagnetic direction rotated around the bedding strike defines a small circle (SC) in equal area projection. (b) The remagnetization direction is common to all sites and therefore it must be the intersection direction of the SCs. (c) One the remagnetization direction is known, it is used as a reference to calculate the best fit (BF) direction and their corresponding paleodip. (d) Small circles and mean-site paleomagnetic direction before bedding correction (BBC) and after total bedding correction (ATBC) of data from the study area (Calvín et al., 2017a). (e) The calculated remagnetization direction (the reference) and the minimum A/n values are coincident with the ca. 100 Ma directions for NW of Africa obtained through the global apparent polar wander path (Torsvik et al., 2012). The remagnetization direction is calculated as the closest direction to a set of small circles, i.e. the direction that minimize A/n. (f) Calculated best fit directions (BFD) used to obtain the paleodips. (g) Bootstrap fold-test (Tauxe and Watson, 1994; Tauxe et al., 2010) of the study area showing a syn-folding behavior of the remagnetization.

Figure DR2. Orthogonal plots of alternating field (Af) and thermal (Th) NRM demagnetization of representative samples in geographic coordinates. Open symbols are projected onto the vertical E-W plane and solid ones in the horizontal plane with N towards the left and W downwards.

Figure DR3. (a) SK19-6 hysteresis loops (original and after subtracting the paramagnetic fraction) and backfield demagnetization curve (b) Hysteresis parameters plot and mixing curves for magnetite (Dunlop, 2002) showing a mixture between SP and SSD. (c) Alternating field demagnetization curves of the NRM and the ARM. (d) ARM/SIRM ratio as function of the strength of the direct biasing field interpreted as SSD magnetite. (e) IRM/SIRM ratio during IRM acquisition and AF demagnetization of the SIRM. Acquisition-demagnetization pairs of curves cross around 0.4. (f) Double IRM acquisition (Mitra et al., 2011), consisting of a double progressive acquisition of IRM. The inset shows the IRAT values (M(z) / M(-z)) for each step.

Table DR1. Summary of location, age of the rocks, attitude of the in situ bedding (So) and the remagnetization time bedding (Paleo-So).

Table DR2. Dataset.

A2. The Small Circle method and the bedding restorations

In the same way that the bedding can be restored according to paleomagnetic data, it is possible to do the same with the geometric features that can be referred to its reference frame inside the rocks, here including sedimentary or tectonic structures. In this work we restore magnetic fabric ellipsoids and we compare them in three different stages: in the present-day attitude, after applying total bedding correction (i.e. restoring the bedding to the horizontal) and after partial bedding correction (i.e. restoring to the paleodip, which is the bedding attitude at the ca. 100 Ma remagnetization time). The used paleodip data were previously obtained (Calvín et al., 2017a) by means of Small Circle (SC) methods.

SC methods (McClelland-Brown, 1983; Surmont et al., 1990; Shipunov, 1997; Waldhör, 1999; Henry et al., 2004; Waldhör and Appel, 2006; Villalaín et al., 1992; 2003, 2016; Calvín et al. 2017b) provide useful workflows with which to analyze secondary synfolding magnetizations, i.e. remagnetizations: (i) the remagnetization direction can be calculated and (ii) the paleodips of the beds (i.e. the bedding attitude at the remagnetization time) can be known.

A small circle (SC) is the projection, in an equal area plot, of the cone defined by a paleomagnetic direction when it is rotated around its bedding strike (Fig. DR1a); in absence of rotation axes other than along the bedding strike, the SC provides the boundaries for the possible directions that the paleomagnetic direction could have presented in previous stages. A set of paleomagnetic sites affected by the same remagnetization must share this paleomagnetic direction, but if they were differentially folded they would show different in situ paleomagnetic directions (Fig. DR1b). However, the SCs of all sites must intersect in the paleomagnetic direction that is common to all of them (Fig. DR1b), i.e. the remagnetization direction (e.g., Villalaín et al., 2016; for review).

The previous statement is true when some initial assumptions are fulfilled: (i) the analyzed sites were remagnetized simultaneously at geological scale, and (ii) only tilting around the bedding strike is responsible for the dispersion of the paleomagnetic directions. Previous works (Torres-López et al., 2014; 2016; Moussaid et al., 2015; Calvín et al., 2017a, 2018) proved the fulfillment of this initial assumptions in the study area.

Once the remagnetization direction is calculated, it becomes in the reference for paleodip calculations. The necessary rotation around the bedding strike to place the paleomagnetic directions in the closest directions (upon their respective SC) to the reference is calculated and therefore the paleodip of the bedding can be obtained (Fig. DR1c).

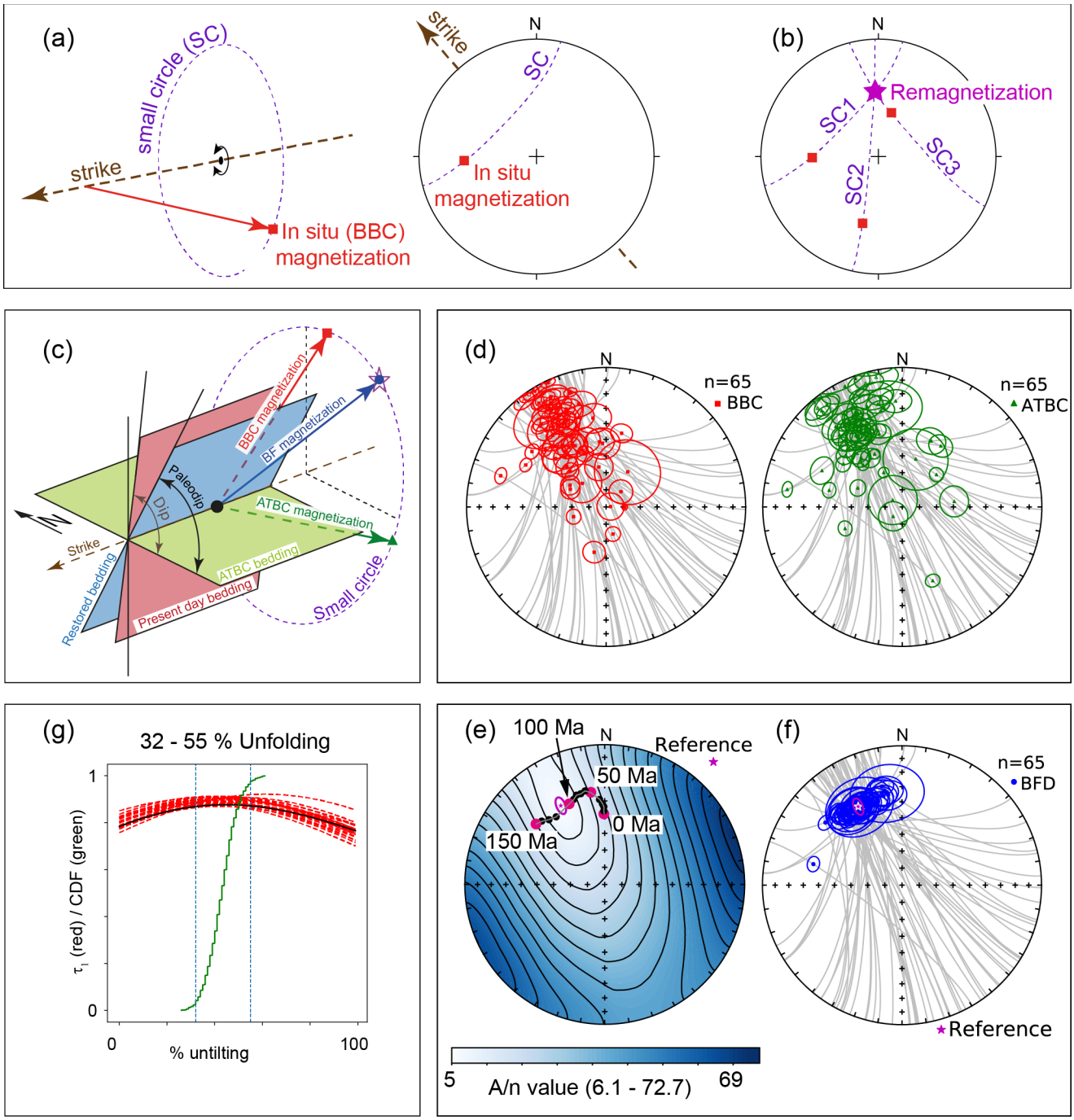

Figure DR1. Charts illustrating the analysis of remagnetization directions using the small circle intersection (SCI) method and bedding restoration at the remagnetization acquisition time. (a) The cone defined by a paleomagnetic direction rotated around the bedding strike defines a small circle (SC) in equal area projection. (b) The remagnetization direction is common to all sites and therefore it must be the intersection direction of the SCs. (c) One the remagnetization direction is known, it is used as a reference to calculate the best fit (BF) direction and their corresponding paleodip. (d) Small circles and mean-site paleomagnetic direction before bedding correction (BBC) and after total bedding correction (ATBC) of data from the study area (Calvín et al., 2017a). (e) The calculated remagnetization direction (the reference) and the minimum A/n values are coincident with the ca. 100 Ma directions for NW of Africa obtained through the global apparent polar wander path (Torsvik et al., 2012). The remagnetization direction is calculated as the closest direction to a set of small circles, i.e. the direction that minimize A/n. (f) Calculated best fit directions (BFD) used to obtain the paleodips. (g) Bootstrap fold-test (Tauxe and Watson, 1994; Tauxe et al., 2010) of the study area showing a syn-folding behavior of the remagnetization.

Twin specimens from the used in this work had been previously analyzed (from a paleomagnetic point of view) by Calvín et al. (2017a). They observed that the limestones carry the regional remagnetization described by Torres-López et al. (2014). It presents the following directional characteristic: site-mean paleomagnetic directions with systematically northwestwards, positive inclinations and scattering both before and after total bedding correction (Fig. DR1d). The remagnetization direction obtained as the SC intersection was calculated (n: 65, Dec: 330.9º, Inc: 35.7º, η: 5.7º, ξ: 2.3º, A/n: 6.12º) using pySCu software (Calvín et al., 2017b) and it is coincident with the ca. 100 Ma. directions for NW of Africa obtained through the global apparent polar wander path (Torsvik et al., 2012) (Fig. DR1e), which was evidenced by Torres-López et al. (2014). The uncertainty in the remagnetization direction is given by the 95% confidence ellipse (Kent, 1982), whose long axis trends NNW-SSE. This agrees with the A/n contour plot (Waldhör and Appel, 2006) (Fig. DR1e), which represents the sum of the angular distances (α) between each direction in the space and the set of SCs ($A=\sum\alpha/n$) and also shows that the uncertainty in the calculation of the remagnetization direction trends NNW-SSE, parallel to the path followed by the SC. Using the remagnetization direction as a reference, the best fit directions (Fig. DR1f), which represent the closest directions to the reference upon each SC are calculated. The necessary rotations around the corresponding bedding strikes from the in situ to the best fit paleomagnetic directions are used to calculate the paleodips.

Furthermore, the synfolding behavior of the remagnetization is also evidenced by the bootstrap fold-test (Tauxe and Watson, 1994) (Fig. DR1g). It is necessary to point out that the synfolding behavior of this remagnetization should not be understood in its classical sense. This remagnetization was not acquired during a folding event, it was acquired during a tectonic quiescence period temporally bracketed between two folding stages (Jurassic extension and Cenozoic compression, respectively) under which the bedding were coaxially folded (e.g. Calvín et al., 2018). Then, in this paper, we refer to it as an interfolding remagnetization.

A3. Rock magnetism of the remagnetized limestones

Previous rock magnetic experiments carried out in the remagnetized limestones of the Central High Atlas (CHA) point out that a mix of superparamagnetic (SP) and stable single domain (SSD) magnetite are the main ferromagnetic s.l. phases present in these rocks (e.g., Torres-López et al., 2014; Calvín et al., 2017a; 2018), being the SSD grains the carriers of the remagnetization.

To complement this information and to characterize the carriers of the ARM several rock magnetic experiment were performed. The natural remanent magnetization (NRM) of twin specimens from those previously treated by thermal demagnetization (Calvín et al., 2017a) were progressively demagnetized by alternating field (AF) using a 755 cryogenic magnetometer (2G) that integrates alternating and direct field coils. Besides, the anhysteretic remanent magnetization (ARM), imparted in

the same samples using a coaxial field of 0.05 mT coupled with a peak alternating field of 90 mT, was also progressively demagnetized by AF. The field window (0-90 mT) in which the ARM was applied (both in the ARM demagnetization and in the measure of the anisotropy of the ARM) is coincident with the coercivity spectra of the neoformed magnetite grains that grew during the remagnetization event. Hysteresis loops and backfield demagnetization curves were measured using a variable field translation balance MMVFTB (Magnetic Measurements) and these data were analyzed with Analyzer 1.1 software (Leonhardt, 2006). The anisotropy of the individual grains of magnetite (multiaxial vs. uniaxial) was tested using the experiment procedures described by Mitra et al. (2011) consisting in the acquisition of a double isothermal remanent magnetization (IRM). For this a double progressive acquisition of IRM is measured, taking two measurements at each field after applying the magnetization along the same axis in opposite directions (i.e. along z and -z). The pair of values are compared with the IRAT parameter, which is the ratio between the magnetization in the second position M(-z) and in the first position M(z). Similar values (i.e. IRAT values close to 1) indicate a dominance of uniaxial grains whereas big differences indicate predominance of multiaxial grains. All of these experiments were performed in the Paleomagnetic Laboratory of Burgos University (Spain). Besides, the progressive acquisition of the ARM was performed at the Institute of Rock Magnetism at the University of Minnesota (USA). Progressive direct fields were imparted in a peak AF of 160 mT with an alternating-field demagnetizer

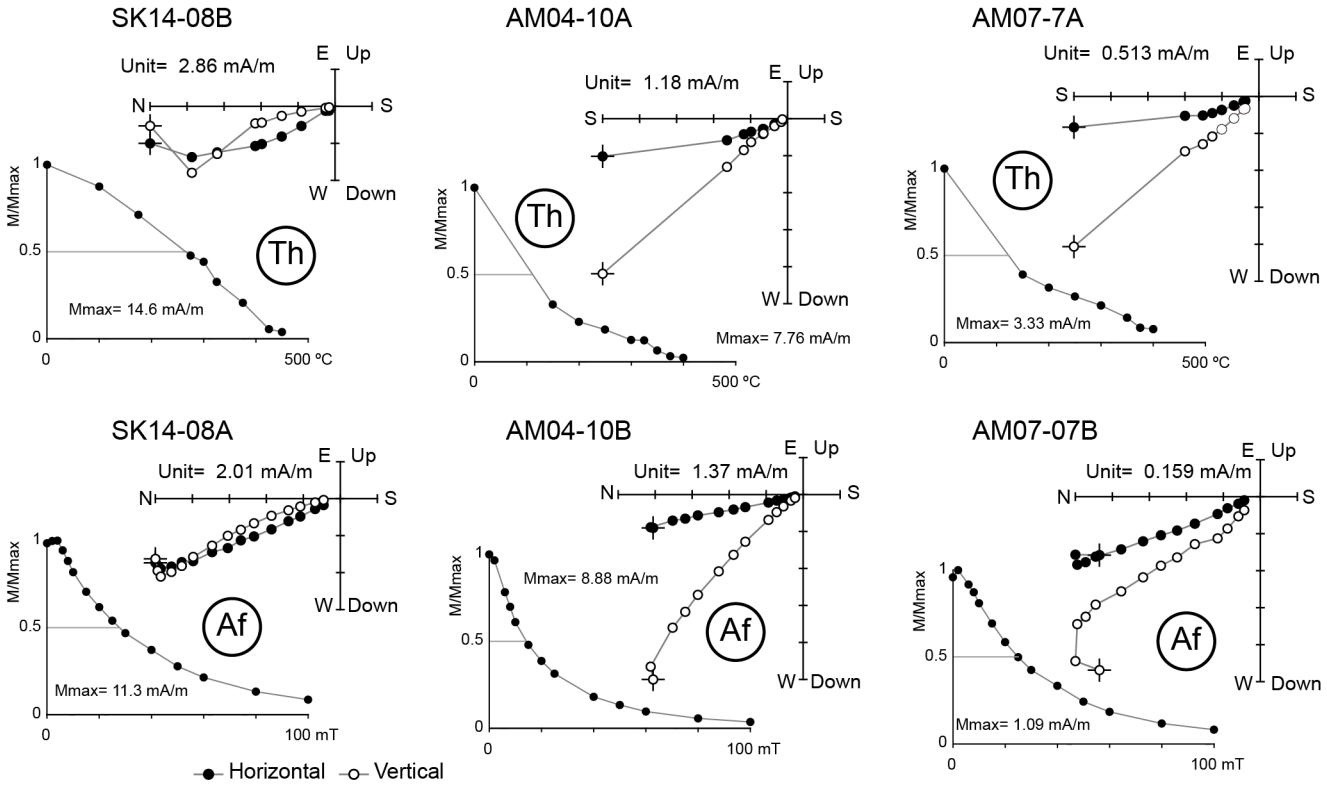

Figure DR2. Orthogonal plots of alternating field (Af) and thermal (Th) NRM demagnetization of representative samples in geographic coordinates. Open symbols are projected onto the vertical E-W plane and solid ones in the horizontal plane with N towards the left and W downwards.

with an ARM device (Schonstedt alternating-field demagnetizer) and measured with a cryogenic 2G magnetometer.

Under thermal demagnetization the NRM shows the remagnetized component with unblocking temperatures between 300 and 450ºC (Fig. DR2). This component is coincident with those observed under AF demagnetization with coercivities between 40-60 and 100 mT. At low coercivities an overlapping can be observed, probably between the remagnetization component and a viscous component. Given the grain distribution typical of remagnetized limestones (e.g., Jackson and Swanson-Hysell, 2012) we interpret that this viscous component is carried by finer magnetite grains (close to the SP behavior) with low relaxation times and therefore genetically related to the SSD magnetite grains that carry the remagnetization.

The SP and SSD mix in remagnetized limestones is evidenced by wasp-waisted hysteresis loops (Fig. DR3a). The hysteresis parameters plot (Fig. DR3b) shows high H_{cr}/H_c ratios (between 5 and 20) that place the measured samples over the SP-SSD experimental curves (Dunlop, 2002). Previous works (e.g. Channel and McCabe, 1994; Jackson and Swanson-Hysell, 2012) in authigenic magnetite-bearing remagnetized limestones reported the same behavior, which is typical of this kind of rocks. Both AF demagnetization curves of NRM and ARM show progressive decays of the magnetization but with different medium destructive fields, with values around 15-20 mT and 25-35 mT respectively. ARM acquisition curves show a nonlinear behavior, reaching over 15 % and 25 % of SIRM for a direct field of 0.2 mT (Fig. DR3d). Similar curves have been interpreted previously as indicative of non-interacting SSD grains (Sugiura, 1979; Jackson and Swanson-Hysell, 2012). This agrees with the cross-point around 0.4 between pairs of IRM acquisition and subsequent AF demagnetization curves (Fig. DR3e) (Cisowski, 1981). Attending to the IRM demagnetization curve (Fig. DR3e), between 10-30% of the initial intensity remains after the AF step of 100 mT, indicating that a minor contribution of high coercivity minerals (probably pyrrhotite and/or goethite) are activate during IRM acquisition. Regarding the shape of the magnetic grains, the forward and reverse isothermal remanent magnetization acquisitions (Fig. DR3f) show negligible differences between the magnetization applied along both z-axis directions, i.e., $M_r(z)$ and $M_r(-z)$, and the ratios between these values (IRAT parameter in the figure) are between 0.9 and 1, indicative of uniaxial particles (Mitra et al., 2011).

In summary, the main magnetic phase of the studied limestones is single domain magnetite distributed in a wide range of size (from SP to SSD), consequence of authigenic growth. Magnetite grains are uniaxial and mostly non-interacting.

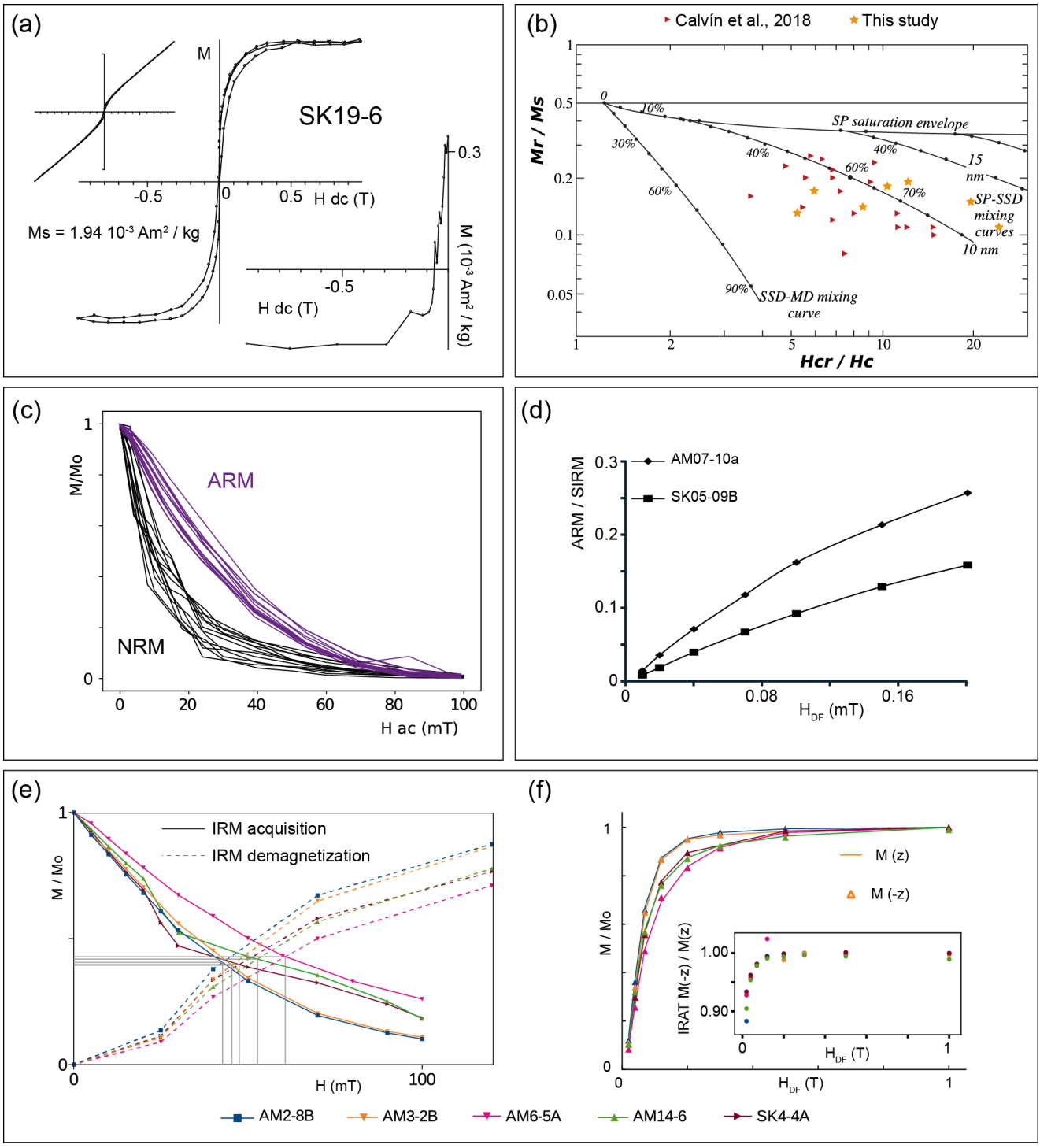

Figure DR3. (a) SK19-6 hysteresis loops (original and after subtracting the paramagnetic fraction) and backfield demagnetization curve (b) Hysteresis parameters plot and mixing curves for magnetite (Dunlop, 2002) showing a mixture between SP and SSD. (c) Alternating field demagnetization curves of the NRM and the ARM. (d) ARM/SIRM ratio as function of the strength of the direct biasing field interpreted as SSD magnetite. (e) IRM/SIRM ratio during IRM acquisition and AF demagnetization of the SIRM. Acquisition-demagnetization pairs of curves cross around 0.4. (f) Double IRM acquisition (Mitra et al., 2011), consisting of a double progressive acquisition of IRM. The inset shows the IRAT values (M(z) / M(-z)) for each step.

A4. References

Calvín, P., Casas-Sainz, A.M., Villalaín, J.J., and Moussaid, B., 2017a, Diachronous folding and cleavage in an intraplate setting (Central High Atlas, Morocco) determined through the study of remagnetizations: Journal of Structural Geology, v. 97, p. 144–160, doi: 10.1016/j.jsg.2017.02.009.

Calvín, P., Villalaín, J.J., Casas-Sainz, A.M., Tauxe, L., and Torres-López, S., 2017b, pySCu: A new python code for analyzing remagnetizations directions by means of small circle utilities: Computers & Geosciences, v. 109, p. 32–42, doi: 10.1016/j.cageo.2017.07.002.

Calvín, P., Casas-Sainz, A.M., Villalaín, J.J., and Moussaid, B., 2018, Extensional vs. compressional deformation in the Central High Atlas salt province: A paleomagnetic approach: Tectonophysics, doi: 10.1016/j.tecto.2018.04.007.

Channell, J.E.T., and McCabe, C., 1994, Comparison of magnetic hysteresis parameters of unremagnetized and remagnetized limestones: Journal of Geophysical Research: Solid Earth, v. 99, p. 4613–4623, doi: 10.1029/93JB02578.

Cisowski, S., 1981, Interacting vs. non-interacting single domain behavior in natural and synthetic samples: Physics of the Earth and Planetary Interiors, v. 26, p. 56–62, doi: 10.1016/0031-9201(81)90097-2.

Dunlop, D.J., 2002, Theory and application of the Day plot (M rs / M s versus H cr / H c) 2. Application to data for rocks, sediments, and soils: Journal of Geophysical Research, v. 107, p. 2057, doi: 10.1029/2001JB000487.

Henry, B., Rouvier, H., and Le Goff, M., 2004, Using syntectonic remagnetizations for fold geometry and vertical axis rotation: the example of the Cévennes border (France): Geophysical Journal International, v. 157, p. 1061–1070, doi: 10.1111/j.1365-246X.2004.02277.x.

Jackson, M., and Swanson-Hysell, N.L., 2012, Rock magnetism of remagnetized carbonate rocks: another look: Geological Society, London, Special Publications, v. 371, p. 229–251, doi: 10.1144/sp371.3.

Kent, J.T., 1982, The Fisher-Bingham distribution on the sphere: Journal of the Royal Statistical Society. Series B, v. 44, p. 71–80, http://www.jstor.org/stable/2984712.

Leonhardt, R., 2006, Analyzing rock magnetic measurements: The RockMagAnalyzer 1.0 software: Computers and Geosciences, v. 32, p. 1420–1431.

McClelland-Brown, E., 1983, Palaeomagnetic studies of fold development and propagation in the Pembrokeshire old red Sandstone: Tectonophysics, v. 98, p. 131–149, doi: 10.1016/0040-1951(83)90214-7.

Mitra, R., Tauxe, L., and Gee, J.S., 2011, Detecting uniaxial single domain grains with a modified IRM technique: Geophysical Journal International, v. 187, p. 1250–1258, doi: 10.1111/j.1365-246X.2011.05224.x.

Moussaid, B., Villalaín, J.J., Casas-Sainz, A., El Ouardi, H., Oliva-Urcia, B., Soto, R., Román-Berdiel, T., and Torres-López, S., 2015, Primary vs. secondary curved fold axes: Deciphering the origin of the Aït Attab syncline (Moroccan High Atlas) using paleomagnetic data: Journal of Structural Geology, v. 70, p. 65–77, doi: 10.1016/j.jsg.2014.11.004.

Shipunov, S. V, 1997, Synfolding magnetization: detection, testing and geological applications: Geophysical Journal International, v. 130, p. 405–410, doi: 10.1111/j.1365-246X.1997.tb05656.x.

Sugiura, N., 1979, ARM, TRM and magnetic interactions: Concentration dependence: Earth and Planetary Science Letters, v. 42, p. 451–455, doi: 10.1016/0012-821X(79)90054-2.

Surmont, J., Sandulescu, M., and Bordea, S., 1990, Mise en évidence dúne réaimantation fini crétacée des séries mésozoïques de l´unité de Bihor (Monts Apuseni, Roumanie) et de sa rotation horarie ultériore: Comptes Rendus De L Academie Des Sciences Paris, v. 310, p. 213–219, http://linkinghub.elsevier.com/retrieve/pii/S1631073X12001926.

Tauxe, L., Shaar, R., Jonestrask, L., Swanson-Hysell, N.L., Minnett, R., Koppers, A.A.P., Constable, C.G., Jarboe, N., Gaastra, K., and Fairchild, L., 2016, PmagPy: Software package for paleomagnetic data analysis and a bridge to the Magnetics Information Consortium (MagIC) Database: Geochemistry, Geophysics, Geosystems, v. 17, p. 2450–2463, doi: 10.1002/2016GC006307.

Tauxe, L., and Watson, G.S., 1994, The fold test: an eigen analysis approach: Earth and Planetary Science Letters, v. 122, p. 331–341, doi: 10.1016/0012-821X(94)90006-X.

Torres-López, S., Villalaín, J.J., Casas, A.M., EL Ouardi, H., Moussaid, B., and Ruiz-Martínez, V.C., 2014, Widespread Cretaceous secondary magnetization in the High Atlas (Morocco). A common origin for the Cretaceous remagnetizations in the western Tethys? Journal of the Geological Society, v. 171, p. 673–687, doi: 10.1144/jgs2013-107.

Torres-López, S., Casas, A.M., Villalaín, J.J., El Ouardi, H., and Moussaid, B., 2016, Pre-Cenomanian vs. Cenozoic folding in the High Atlas revealed by palaeomagnetic data: Terra Nova, v. 28, p. 110–119, doi: 10.1111/ter.12197.

Torsvik, T.H., Van der Voo, R., Preeden, U., Niocaill, C. Mac, Steinberger, B., Doubrovine, P. V., van Hinsbergen, D.J.J., Domeier, M., Gaina, C., Tohver, E., Meert, J.G., McCausland, P.J. a, and Cocks, L.R.M., 2012, Phanerozoic polar wander, palaeogeography and dynamics: Earth-Science Reviews, v. 114, p. 325–368, doi: 10.1016/j.earscirev.2012.06.002.

Villalaín, J.J., Osete, M.L., Vegas, R., and García-Dueñas, V., 1992, Evidencia de una reimanación terciaria en la Béticas Occidentales. Implicaciones tectónicas: Física de la Tierra, v. 4, p. 165–184.

Villalaín, J., Fernández-González, G., Casas, A.M., and Gil-Imaz, A., 2003, Evidence of a Cretaceous remagnetization in the Cameros Basin (North Spain): implications for basin geometry: Tectonophysics, v. 377, p. 101–117, doi: 10.1016/j.tecto.2003.08.024.

Villalaín, J.J., Casas-Sainz, A.M., and Soto, R., 2016, Reconstruction of inverted sedimentary basins from syn-tectonic remagnetizations. A methodological proposal: Geological Society, London, Special Publications, v. 425, p. 233–246, doi: 10.1144/SP425.10.

Waldhör, M., 1999, The small-circle reconstruction in palaeomagnetism and its application to palaeomagnetic data from the pamirs: Tübingen University, 99 p.

Waldhör, M., and Appel, E., 2006, Intersections of remanence small circles: new tools to improve data processing and interpretation in palaeomagnetism: Geophysical Journal International, v. 166, p. 33–45, doi: 10.1111/j.1365-246X.2006.02898.x.

Table DR1. Summary of location, age of the rocks, attitude of the in situ bedding (So) and the remagnetization time bedding (Paleo-So). Bedding data as dip direction and dip. This data come from Calvín et al. (2017).

Site	Longitude (WGS84)	Latitude (WGS84)	Age	So : DD/Dip	Paleo-So : DD/Dip
AM02	5° 03' 14.2934" W	32° 13' 48.5580" N	Bajocian	175/60	175/24
AM03	5° 01' 44.8230" W	32° 14' 5.4535" N	Bajocian	170/53	170/31
AM04	5° 01' 55.5442" W	32° 16' 22.3799" N	Aalenian-Bajocian	191/22	191/22
AM06	4° 57' 39.8714" W	32° 17' 45.8084" N	Toarcian-Aalenian	134/32	134/08
AM07	4° 45' 19.9271" W	32° 16' 18.5563" N	Bajocian	318/26	318/13
AM08	4° 48' 34.0337" W	32° 15' 54.8597" N	Aalenian-Bajocian	150/52	150/49
AM13	4° 49' 11.5072" W	32° 16' 19.0200" N	Bajocian	148/34	148/20
AM14	5° 06' 7.0200" W	32° 16' 34.1400" N	Aalenian-Bajocian	353/46	353/09
SK04	5° 28' 44.4918" W	32° 04' 32.8883" N	Aalenian-Bajocian	015/20	015/05
SK05	5° 28' 5.5963" W	32° 02' 37.0194" N	Aalenian-Bajocian	333/48	333/26
SK07	5° 28' 7.6602" W	32° 02' 19.0704" N	Aalenian-Bajocian	160/14	160/05
SK14	5° 19' 31.1365" W	32° 08' 53.5823" N	Toarcian-Aalenian	180/64	180/38
SK19	5° 22' 48.4997" W	32° 07' 49.3291" N	Aalenian-Bajocian	177/28	177/20

Table DR2.

		Orientation of the principal axes (In situ)						k (1981) parameters		AARM tensor components (In situ)						Eigenvalues of the principal axes			Bulk AARM susceptibility (SI)	% RMS error
SITE	SAMPLE	K1_DEC	K1_INC	K2_DEC	K2_INC	K3_DEC	K3_INC	Pj	T	kxx	kyy	kzz	kxy	kyz	kxz	k_max	k_int	k_min	k_mean	RMS(resid)/RMS(ARM) (%)
AM02	AM02-03A	167.65	24.03	346.25	65.97	77.42	0.52	1.038	-0.84	3.33E-05	3.24E-05	3.27E-05	-2.00E-07	8.00E-08	-3.80E-07	3.35E-05	3.25E-05	3.24E-05	3.28E-05	0.12%
AM02	AM02-4B	140.08	18.48	253.76	50.24	37.18	33.74	1.030	0.04	7.10E-05	7.11E-05	7.10E-05	-6.10E-07	-2.70E-07	-5.20E-07	7.17E-05	7.13E-05	7.01E-05	7.10E-05	0.12%
AM02	AM02-05B	181.56	37.50	287.73	19.95	39.60	45.74	1.034	-0.32	3.84E-05	3.81E-05	3.82E-05	-1.20E-07	-1.90E-07	-5.10E-07	3.88E-05	3.82E-05	3.77E-05	3.82E-05	0.40%
AM02	AM02-07A	159.69	24.89	67.44	4.82	327.21	64.59	1.029	-0.67	1.18E-04	1.16E-04	1.16E-04	-6.80E-07	5.40E-07	-1.01E-06	1.19E-04	1.16E-04	1.15E-04	1.17E-04	0.15%
AM02	AM02-08B	179.94	27.09	51.48	50.57	284.57	26.29	1.025	0.49	2.70E-04	2.65E-04	2.67E-04	5.00E-07	9.90E-07	-2.39E-06	2.71E-04	2.66E-04	2.64E-04	2.67E-04	0.25%
AM03	AM03-02B	335.18	10.92	190.36	76.72	66.63	7.47	1.026	-0.40	6.50E-04	6.40E-04	6.44E-04	-6.07E-06	-1.58E-06	1.31E-06	6.53E-04	6.43E-04	6.36E-04	6.44E-04	0.23%
AM03	AM03-04A	343.23	18.18	147.64	71.17	251.68	4.73	1.025	-0.71	6.33E-04	6.22E-04	6.25E-04	-3.93E-06	-9.30E-07	3.69E-06	6.35E-04	6.23E-04	6.20E-04	6.26E-04	0.20%
AM03	AM03-07A	327.16	29.43	174.52	57.57	64.28	12.39	1.032	-0.07	6.50E-04	6.41E-04	6.48E-04	-7.32E-06	-4.28E-06	2.85E-06	6.56E-04	6.46E-04	6.37E-04	6.46E-04	0.23%
AM03	AM03-08A	200.88	9.30	295.07	24.04	91.26	64.01	1.028	0.36	3.82E-04	3.77E-04	3.72E-04	1.11E-06	-3.59E-06	-5.40E-07	3.82E-04	3.78E-04	3.70E-04	3.77E-04	0.32%
AM04	AM04-05A	182.43	8.65	90.78	10.67	310.72	76.20	1.041	-0.42	4.03E-04	3.92E-04	3.89E-04	7.50E-07	6.10E-07	-2.26E-06	4.04E-04	3.92E-04	3.88E-04	3.94E-04	0.33%
AM04	AM04-07A	143.03	12.98	235.99	12.63	8.73	71.73	1.027	0.13	2.54E-04	2.54E-04	2.49E-04	-1.87E-06	3.30E-07	-1.67E-06	2.56E-04	2.52E-04	2.49E-04	2.52E-04	0.31%
AM04	AM04-08A	171.88	17.51	80.98	2.87	341.98	72.24	1.050	-0.58	5.27E-04	5.11E-04	5.07E-04	-2.38E-06	1.28E-06	-6.97E-06	5.30E-04	5.10E-04	5.05E-04	5.15E-04	0.30%
AM04	AM04-09A	159.19	16.49	250.96	5.96	0.16	72.41	1.046	-0.22	5.64E-04	5.53E-04	5.44E-04	-5.01E-06	1.58E-06	-6.80E-06	5.68E-04	5.51E-04	5.42E-04	5.54E-04	0.23%
AM04	AM04-10B	178.34	17.38	271.82	10.98	32.63	69.25	1.052	-0.46	9.99E-04	9.69E-04	9.61E-04	-1.60E-06	-2.13E-06	-1.33E-05	1.00E-03	9.69E-04	9.56E-04	9.76E-04	0.27%
AM06	AM06-01A	163.93	29.49	71.50	4.29	333.98	60.14	1.050	-0.01	2.45E-04	2.42E-04	2.39E-04	-7.00E-07	1.84E-06	-4.66E-06	2.48E-04	2.42E-04	2.36E-04	2.42E-04	0.20%
AM06	AM06-02A	167.36	27.78	71.40	11.15	321.70	59.69	1.047	0.16	2.95E-04	2.91E-04	2.88E-04	7.00E-08	2.32E-06	-4.79E-06	2.97E-04	2.92E-04	2.84E-04	2.91E-04	0.35%
AM06	AM06-03A	146.99	24.11	54.16	6.28	310.52	64.98	1.050	0.31	3.38E-04	3.36E-04	3.28E-04	-8.10E-07	4.21E-06	-4.46E-06	3.41E-04	3.36E-04	3.25E-04	3.34E-04	0.24%
AM06	AM06-04A	153.19	23.49	60.72	5.65	318.02	65.76	1.050	0.15	4.26E-04	4.22E-04	4.13E-04	-2.28E-06	4.12E-06	-6.16E-06	4.30E-04	4.21E-04	4.10E-04	4.20E-04	0.12%
AM06	AM06-05A	142.93	27.89	246.93	24.56	11.65	51.26	1.033	-0.89	5.71E-04	5.69E-04	5.66E-04	-5.74E-06	3.27E-06	-6.25E-06	5.79E-04	5.65E-04	5.61E-04	5.68E-04	0.19%
AM07	AM07-01A	176.97	13.91	65.36	56.07	275.27	30.24	1.040	-0.73	4.10E-04	3.97E-04	3.99E-04	-2.80E-07	1.16E-06	-2.58E-06	4.10E-04	3.99E-04	3.97E-04	4.02E-04	0.18%
AM07	AM07-05A	358.62	0.56	89.01	35.09	267.83	54.91	1.038	-0.45	6.36E-04	6.17E-04	6.15E-04	-5.90E-07	3.04E-06	2.10E-07	6.36E-04	6.19E-04	6.13E-04	6.23E-04	0.21%
AM07	AM07-06A	186.64	4.76	90.73	51.02	280.45	38.57	1.048	-0.27	3.31E-04	3.19E-04	3.20E-04	1.38E-06	1.83E-06	-1.22E-06	3.32E-04	3.21E-04	3.17E-04	3.23E-04	0.58%
AM07	AM07-07B	168.16	16.93	66.23	34.17	280.04	50.75	1.031	-0.55	4.05E-04	3.96E-04	3.96E-04	-1.70E-06	1.09E-06	-2.48E-06	4.06E-04	3.96E-04	3.95E-04	3.99E-04	0.17%
AM07	AM07-10A	2.51	22.98	220.94	61.57	99.40	15.81	1.032	-0.57	5.66E-04	5.52E-04	5.56E-04	7.70E-07	-3.40E-07	5.11E-06	5.68E-04	5.54E-04	5.52E-04	5.58E-04	0.64%
AM08	AM08-02A	156.48	11.28	249.45	14.56	30.05	71.42	1.063	-0.27	1.44E-04	1.41E-04	1.38E-04	-2.06E-06	-1.70E-07	-1.79E-06	1.45E-04	1.40E-04	1.37E-04	1.41E-04	0.15%
AM08	AM08-03A	160.24	12.12	250.86	2.90	354.09	77.53	1.063	-0.14	1.21E-04	1.18E-04	1.15E-04	-1.24E-06	1.50E-07	-1.59E-06	1.22E-04	1.18E-04	1.14E-04	1.18E-04	0.16%
AM08	AM08-04A	153.40	10.63	244.63	6.53	5.69	77.48	1.067	0.01	1.76E-04	1.73E-04	1.67E-04	-2.41E-06	1.50E-07	-2.28E-06	1.78E-04	1.72E-04	1.66E-04	1.72E-04	0.12%
AM08	AM08-06A	171.89	12.03	263.17	6.01	19.21	76.51	1.069	-0.16	8.24E-05	7.96E-05	7.76E-05	-4.60E-07	-5.00E-08	-1.06E-06	8.26E-05	7.95E-05	7.74E-05	7.98E-05	0.07%
AM08	AM08-09A	159.81	15.35	255.41	19.56	34.25	64.73	1.055	-0.50	1.14E-04	1.11E-04	1.10E-04	-1.49E-06	-2.70E-07	-1.62E-06	1.15E-04	1.11E-04	1.09E-04	1.12E-04	0.16%
AM13	AM13-03A	160.54	25.49	352.05	64.05	252.70	4.52	1.023	-0.80	2.62E-04	2.58E-04	2.59E-04	-1.36E-06	8.10E-07	-1.53E-06	2.63E-04	2.59E-04	2.58E-04	2.60E-04	0.32%
AM13	AM13-04B	174.01	17.77	306.13	64.46	78.13	17.73	1.021	-0.28	3.92E-04	3.85E-04	3.88E-04	-8.60E-07	-8.00E-07	-1.77E-06	3.93E-04	3.87E-04	3.85E-04	3.88E-04	0.19%
AM13	AM13-06A	177.82	9.05	283.66	59.74	82.84	28.60	1.024	-0.19	1.79E-03	1.75E-03	1.76E-03	-2.25E-06	-4.41E-06	-2.31E-06	1.79E-03	1.76E-03	1.75E-03	1.77E-03	0.12%
AM13	AM13-07A	165.62	10.33	270.16	53.99	68.55	34.04	1.026	0.11	2.56E-03	2.52E-03	2.52E-03	-1.72E-05	-1.26E-05	-9.11E-06	2.57E-03	2.54E-03	2.50E-03	2.53E-03	0.26%
AM13	AM13-08A	193.93	10.80	290.40	30.58	86.74	57.17	1.026	0.74	1.29E-03	1.28E-03	1.27E-03	1.32E-06	-1.19E-05	-1.31E-06	1.29E-03	1.29E-03	1.26E-03	1.28E-03	0.16%
AM14	AM14-04A	334.69	25.52	71.48	13.92	187.39	60.44	1.048	-0.52	1.09E-03	1.07E-03	1.06E-03	-1.08E-05	-5.28E-06	1.83E-05	1.10E-03	1.06E-03	1.05E-03	1.07E-03	0.12%
AM14	AM14-05A	328.42	33.47	234.82	5.42	136.75	55.97	1.045	-0.35	1.37E-03	1.36E-03	1.35E-03	-8.96E-06	-1.57E-05	2.12E-05	1.39E-03	1.35E-03	1.33E-03	1.36E-03	0.20%
AM14	AM14-06A	339.29	35.87	72.15	3.94	167.56	53.84	1.058	-0.67	1.59E-03	1.56E-03	1.57E-03	-1.38E-05	-1.27E-05	3.77E-05	1.62E-03	1.55E-03	1.54E-03	1.57E-03	0.48%
AM14	AM14-07A	319.15	16.77	66.95	45.41	214.61	39.79	1.043	-0.37	9.81E-04	9.80E-04	9.68E-04	-1.59E-05	-1.61E-06	1.06E-05	9.99E-04	9.71E-04	9.59E-04	9.77E-04	0.16%
AM14	AM14-08A	348.21	11.65	257.63	2.82	154.23	78.00	1.051	-0.08	8.26E-04	8.07E-04	7.89E-04	-3.95E-06	-2.52E-06	7.75E-06	8.28E-04	8.06E-04	7.87E-04	8.07E-04	1.28%
SK04	SK04-4A	334.06	11.87	236.61	31.66	81.99	55.68	1.024	-0.23	1.46E-04	1.44E-04	1.43E-04	-7.90E-07	-7.40E-07	-8.00E-08	1.46E-04	1.44E-04	1.43E-04	1.44E-04	0.12%
SK04	SK04-08A	308.18	16.43	41.20	10.16	161.65	70.53	1.051	0.47	1.54E-04	1.55E-04	1.49E-04	-5.90E-07	-8.90E-07	1.84E-06	1.56E-04	1.54E-04	1.48E-04	1.53E-04	0.41%
SK04	SK04-9A	323.72	28.42	233.14	1.07	141.16	61.55	1.052	-0.09	1.22E-04	1.22E-04	1.21E-04	-1.30E-07	-5.00E-07	6.70E-07	1.23E-04	1.22E-04	1.21E-04	1.22E-04	0.29%
SK04	SK04-10A	307.02	2.75	37.41	8.07	198.33	81.46	1.040	0.44	1.16E-04	1.17E-04	1.12E-04	-1.62E-06	6.00E-08	9.00E-08	1.18E-04	1.15E-04	1.12E-04	1.15E-04	0.46%
SK04	SK04-11A	298.74	1.72	28.95	6.84	194.69	82.95	1.016	0.19	7.30E-05	7.35E-05	7.09E-05	-3.70E-07	4.00E-08	2.40E-07	7.37E-05	7.29E-05	7.09E-05	7.25E-05	0.27%
SK05	SK05-01A	335.08	8.63	244.62	3.05	135.32	80.84	1.054	0.23	1.15E-04	1.13E-04	1.10E-04	-9.80E-07	-5.30E-07	7.00E-07	1.16E-04	1.13E-04	1.10E-04	1.13E-04	0.14%
SK05	SK05-02A	329.27	10.49	60.57	6.99	183.69	77.35	1.049	-0.32	3.65E-04	3.59E-04	3.52E-04	-5.05E-06	-1.20E-06	2.83E-06	3.69E-04	3.56E-04	3.52E-04	3.59E-04	0.22%
SK05	SK05-05C	306.32	8.86	37.86	9.81	174.97	76.72	1.038	0.27	2.16E-04	2.18E-04	2.11E-04	-1.32E-06	-6.50E-07	1.38E-06	2.18E-04	2.16E-04	2.11E-04	2.15E-04	0.32%
SK05	SK05-06B	256.99	9.55	158.48	41.34	357.41	47.07	1.038	0.38	1.12E-04	1.14E-04	1.12E-04	2.80E-07	-3.00E-08	-1.44E-06	1.14E-04	1.13E-04	1.10E-04	1.13E-04	0.13%
SK05	SK05-09A	337.33	28.66	245.96	2.51	151.39	61.21	1.058	0.22	3.84E-04	3.81E-04	3.73E-04	-1.15E-06	-3.89E-06	7.86E-06	3.89E-04	3.81E-04	3.69E-04	3.80E-04	0.34%
SK07	SK07-01A	162.57	21.07	66.91	14.37	305.07	64.10	1.107	0.27	1.63E-04	1.59E-04	1.52E-04	-4.10E-07	3.53E-06	-4.24E-06	1.65E-04	1.59E-04	1.50E-04	1.58E-04	0.22%
SK07	SK07-02B	161.20	15.38	67.89	11.85	301.78	70.40	1.112	-0.15	4.46E-04	4.25E-04	4.10E-04	-6.64E-06	7.16E-06	-9.32E-06	4.51E-04	4.24E-04	4.06E-04	4.27E-04	0.20%
SK07	SK07-04B	167.30	17.80	70.80	19.44	296.63	63.14	1.099	-0.31	3.80E-04	3.59E-04	3.54E-04	-3.79E-06	5.13E-06	-8.58E-06	3.83E-04	3.60E-04	3.49E-04	3.64E-04	0.21%
SK07	SK07-07B	172.55	18.81	75.27	20.42	301.67	61.64	1.079	-0.51	3.08E-04	2.91E-04	2.90E-04	-1.79E-06	2.26E-06	-6.43E-06	3.10E-04	2.92E-04	2.88E-04	2.97E-04	0.15%
SK07	SK07-08C	167.54	12.87	69.27	32.18	276.39	54.74	1.100	-0.33	5.20E-04	4.88E-04	4.84E-04	-6.09E-06	7.79E-06	-7.69E-06	5.23E-04	4.91E-04	4.77E-04	4.97E-04	0.32%

SK14	SK14-07B	162.61	39.28	257.04	5.39	353.55	50.20	1.048	-0.38	5.96E-04	5.90E-04	5.92E-04	-3.13E-06	3.49E-06	-1.32E-05	6.09E-04	5.89E-04	5.81E-04	5.93E-04	0.09%
SK14	SK14-08A	168.39	32.28	46.27	40.09	282.83	33.22	1.025	-0.49	2.18E-03	2.14E-03	2.16E-03	-2.97E-06	1.45E-05	-2.35E-05	2.20E-03	2.15E-03	2.13E-03	2.16E-03	0.18%
SK14	SK14-12A	179.63	23.55	81.20	18.61	316.73	59.25	1.031	0.18	1.66E-03	1.64E-03	1.64E-03	1.40E-06	4.81E-06	-1.41E-05	1.67E-03	1.64E-03	1.63E-03	1.65E-03	0.12%
SK14	SK14-14A	190.74	7.42	98.36	17.68	302.60	70.73	1.031	-0.06	1.37E-03	1.36E-03	1.34E-03	4.73E-06	7.82E-06	-6.46E-06	1.38E-03	1.36E-03	1.33E-03	1.36E-03	0.17%
SK19	SK19-01A	121.73	28.29	241.69	42.86	10.44	34.00	1.015	0.09	3.51E-04	3.57E-04	3.53E-04	-2.67E-06	1.70E-06	-3.65E-06	3.59E-04	3.53E-04	3.48E-04	3.54E-04	0.22%
SK19	SK19-05A	148.82	2.86	48.08	74.98	239.58	14.73	1.027	-0.21	4.80E-04	4.76E-04	4.79E-04	-3.35E-06	1.18E-06	5.00E-07	4.82E-04	4.79E-04	4.74E-04	4.78E-04	0.38%
SK19	SK19-06	339.62	2.35	241.68	73.42	70.31	16.40	1.027	-0.21	4.87E-04	4.77E-04	4.80E-04	-3.63E-06	-1.28E-06	-2.50E-07	4.88E-04	4.80E-04	4.75E-04	4.81E-04	0.25%
SK19	SK19-07B	315.83	6.73	68.63	73.07	223.96	15.46	1.019	-0.05	1.00E-03	1.00E-03	9.95E-04	-1.86E-05	-2.92E-06	6.11E-06	1.02E-03	9.96E-04	9.82E-04	1.00E-03	0.17%
SK19	SK19-08A	144.95	36.81	271.26	38.36	28.92	30.39	1.024	0.17	5.71E-04	5.72E-04	5.73E-04	-4.37E-06	-1.90E-07	-5.25E-06	5.78E-04	5.73E-04	5.65E-04	5.72E-04	0.41%